Patterns and quasi-patterns in the Faraday experiment

By W. S. EDWARDS[1] AND S. FAUVE[2]

[1] Department of Physics, Haverford College, Haverford, PA 19041, USA

[2] Laboratoire de Physique, Ecole Normalie Supérieure de Lyon, 46, allée d'Italie, 69364 Lyon Cedex 07, France

Parametric excitation of surface waves via forced vertical oscillation of a container filled with fluid (the Faraday instability) is investigated experimentally in a small-depth large-aspect-ratio system, with a viscous fluid and with two simultaneous forcing frequencies. The asymptotic pattern observed just above the threshold for the first instability of the flat surface is found to depend strongly on the frequency ratio and the amplitudes and phases of the two sinusoidal components of the driving acceleration. Parallel lines, squares, and hexagons are observed. With viscosity 100 cS, these stable standing-wave patterns do not exhibit strong sidewall effects, and are found in containers of various shapes including an irregular shape. A 'quasi-pattern' of twelvefold symmetry, analogous to a two-dimensional quasi-crystal, is observed for some even/odd frequency ratios. Many of the experimental phenomena can be modelled via cubic-order amplitude equations derived from symmetry arguments.

1. Introduction

Pattern-forming instabilities occur in a variety of continuum-mechanical situations including many hydrodynamic experiments. The behaviour of such patterns is often governed by amplitude equations whose form depends on the symmetries of the problem but is otherwise largely independent of the hydrodynamic details. These equations, and the methodology that accompanies them, provide a common framework for the analysis of many otherwise disparate physical systems (cf. the recent reviews of Newell, Passot and Lega 1993 and Cross & Hohenberg 1993). The most often studied example of such a pattern-forming system is Rayleigh–Bénard convection.

This article reports experimental investigations of the Faraday instability (Faraday 1831), in which a container of fluid with a free upper surface is subject to vertical oscillation. The system undergoes a pattern-forming instability when the amplitude of the vertical forcing exceeds a critical value. All previous theoretical and experimental studies of this instability have been based on sinusoidal forcing. Here, the problem is generalized to the case of two simultaneous forcing frequencies.

It appears likely that the results of these experiments can be understood on the basis of a nonlinear analysis for a horizontally infinite system, ignoring sidewalls. This leads to amplitude equations for certain sets of standing-wave Fourier modes, as for example in the theories of Ezerskii *et al.* (1986), Milner (1991), and Miles (1993). Considerable effort will be required, however, to generalize these theories to take into account two (or more) forcing frequencies.

In contrast to most previous experiments, a viscous fluid is used. This ensures that patterns are not strongly sensitive to sidewall geometry, as is common for Faraday

experiments in low-viscosity fluids such as water. Also, the depth of the fluid layer is comparable to the wavelength, while in almost all previous work the depth is much larger than the wavelength in order to approach the infinite-depth limit. The small depth is intended to suppress long-wavelength instabilities that make it difficult to obtain stable homogeneous patterns over wide parameter ranges.

The article begins with a section on theoretical motivations. A discussion of the hydrodynamic stability problem and its symmetries is given, and the forms of amplitude equations for spatially homogeneous patterns of standing waves are presented. Of particular interest is the concept of bicriticality of wavenumbers and the possibility of deliberate selection of geometrically interesting patterns via appropriate choices of frequency ratios and other parameters.

Subsequent sections describe the experimental apparatus and then report and discuss the experimental results obtained with single-frequency and two-frequency forcing. In the latter case a novel 'quasi-pattern' with twelvefold symmetry (Edwards & Fauve 1992, 1993) is found. The existence of such a structure demonstrates that quasi-crystalline order can arise in a purely continuum-mechanical system where spatially localized objects such as atoms or tiles do not appear to be a necessary aspect of the theoretical treatment. The mathematical analysis of quasi-patterns is similar to that of spatially regular patterns such as squares or hexagons, and has features in common with density-wave models of quasi-crystals.

The term 'quasi-pattern' refers to a pattern with long-range orientational order but no spatial periodicity, thus analogous to a quasi-crystal, but arising spontaneously in a nonlinear continuum-mechanical system having the symmetries of the (horizontal) plane. The physical system is translationally, rotationally and parity invariant ('parity' here means with respect to reflections through vertical planes), and the quasi-pattern arises via a symmetry-breaking bifurcation with finite critical wavenumber. Excluded from this definition are patterns arising in spatially forced or inhomogeneous systems and patterns due essentially to effects of sidewall geometry.

A necessary theoretical complement to this work will be the calculation, directly from the governing hydrodynamic equations, of the standing-wave patterns and quasi-patterns. The multiple-frequency Faraday experiment presents a unique opportunity to completely characterize and quantify the interactions among periodic and quasi-periodic patterns in the plane, in a physical and mathematical problem that is simply and cleanly defined. Progress in this direction has been made recently by Kumar & Tuckerman (1994), and Tuckerman, Kumar & Edwards (1994), although the full nonlinear calculation has not yet been attempted.

2. Theoretical motivations

2.1. *General remarks*

The hydrodynamic problem concerns the stability of the flat free upper surface of an incompressible Newtonian fluid, of density ρ, kinematic viscosity ν, and surface tension σ, when the container is forced to oscillate vertically. The experiment is depicted schematically in figure 1. When the amplitude of the forcing acceleration $f(t)$ exceeds a critical threshold, the flat surface becomes unstable and a pattern of standing waves appears.

The simplest and most often studied case is that of a sinusoidal forcing function $f(t) = a\cos(2\omega t)$ for a fluid of small viscosity ν. Benjamin & Ursell (1954), starting with the ideal fluid equations, showed that in the linear stability problem the surface deformation for each standing-wave Fourier mode, having horizontal wavevector
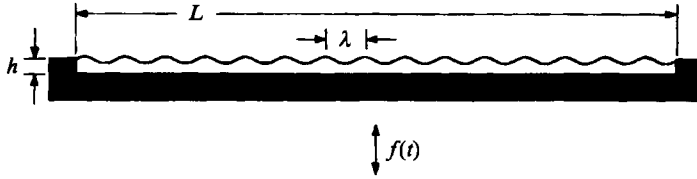
FIGURE 1. Basic hydrodynamic problem. A rigid container of depth h and horizontal dimension L (in both horizontal directions) is filled with an incompressible Newtonian fluid of density ρ and kinematic viscosity ν. The surface tension on the free upper surface is σ. The container is subjected to oscillatory vertical acceleration $f(t)$. Standing waves of wavelength λ appear on the surface when the amplitude a of the forcing exceeds a threshold value a_c.
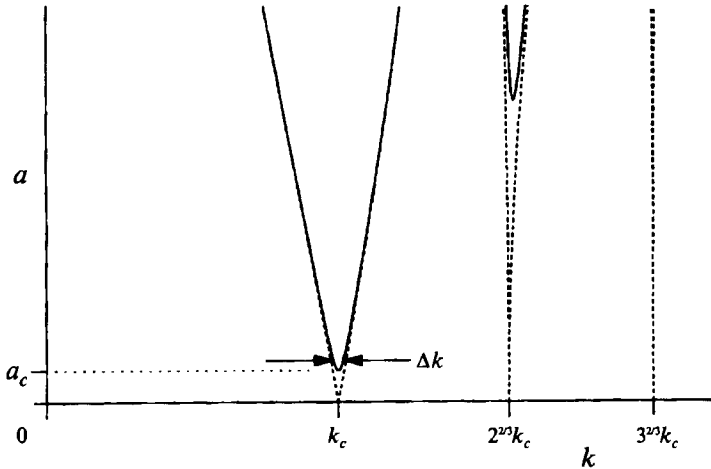

FIGURE 2. Resonance tongues for the Faraday problem with $f(t) = a\cos(2\omega t)$, from tabulated results for the Mathieu equation, are shown for the infinite-depth capillary dispersion relation $\omega_0^2 = (\sigma/\rho)k^3$. Dashed lines are inviscid stability boundaries. Solid lines are stability boundaries for a small viscosity ν, with damping $\delta = 2\nu k^2$. The critical forcing acceleration is a_c for the subharmonic tongue at k_c. The band of unstable wavenumbers Δk is shown here for $\mu \equiv (a-a_c)/a_c = 0.3$.

$\boldsymbol{k} = k_x \hat{\boldsymbol{e}}_x + k_y \hat{\boldsymbol{e}}_y$, is $\hat{\zeta}(t)\exp(\mathrm{i}\boldsymbol{k}\cdot\boldsymbol{x}) + \text{c.c.}$, where $\hat{\zeta}(t)$ is a real-valued function obeying the Mathieu equation

$$\partial_t^2 \hat{\zeta} = -\omega_0^2 \hat{\zeta} + ak\tanh(kh)\cos(2\omega t)\hat{\zeta} \tag{1}$$

with $k = |\boldsymbol{k}| = 2\pi/\lambda$. The natural resonant frequency ω_0 is given by the dispersion relation

$$\omega_0^2(k) = \tanh(kh)\left[gk + \frac{\sigma}{\rho}k^3\right], \tag{2}$$

where g is the acceleration due to gravity. The *infinite-depth limit* corresponds to $\tanh(kh) \to 1$. When the term gk dominates the sum, the mode is a *gravity wave*, and when $(\sigma/\rho)k^3$ dominates it is a *capillary wave*.

Analysis of the Mathieu equation yields a set of resonance tongues, the first three of which are shown in figure 2. A decay rate δ can be calculated to first order in ν by integrating the viscous energy dissipation in the eigenmode obtained from the inviscid calculation. For infinite depth this decay rate is $\delta = 2\nu k^2$ (cf. Milner 1991). A phenomenological damping term is added to the Mathieu equation, which becomes

$$\partial_t^2 \hat{\zeta} = -\omega_0^2 \hat{\zeta} + ak\cos(2\omega t)\hat{\zeta} - 2\delta\,\partial_t\hat{\zeta}. \tag{3}$$

This leads to finite stability thresholds for each tongue, the lowest of which is, in the infinite-depth and capillary limits, $a_c = 8\omega k_c \nu$ for the *subharmonic* response at k_c such that $\omega_0(k_c) = \omega$, i.e. half the drive frequency. (In the case of a layer of fluid of finite depth, (3) is phenomenological and cannot be derived from the Navier–Stokes equations even in the small-viscosity limit. There is an additional integro-differential term which contributes to the dissipation like $(\nu\omega)^{1/2}k/(\cosh kh \sinh kh)$.)

2.2. *The low-viscosity limit and finite-size effects*

Benjamin & Ursell's linear analysis is simplified by the use of the ideal fluid equations, with viscosity treated as a perturbation. The study of pattern selection, however, requires a nonlinear analysis (Ezerskii *et al.* 1986; Milner 1991; Miles 1993) which, like the linear theory, is considerably simplified if it can be performed for a horizontally infinite system, ignoring sidewalls. This motivates experiments with large horizontal size L. It might be expected that sidewall effects are negligible when $L \gg \lambda$, and that small-viscosity theory for the infinite plane would accurately predict the selected pattern for all such 'large aspect-ratio' experiments.

However, for small viscosity the linear problem is very sensitive to the quantization imposed by the finite container size L. The instability ocurs near the bottom of the (inviscid) subharmonic tongue, where the width Δk of the band of unstable wavenumbers is small, going to zero as $\nu \to 0$. The patterns that develop for small values of the bifurcation parameter $\mu \equiv (a-a_c)/a_c$ will be insensitive to container size and shape only when Δk is much larger than π/L, the wavenumber separation between quantized modes of the container.

Figure 2 shows neutral curves for both the inviscid case and for small viscosity ν. In the infinite-depth capillary limits, the width Δk of the band of unstable wavenumbers is given by

$$\Delta k = \frac{8\sqrt{2}}{3}\frac{\rho\nu}{\sigma}\omega\mu^{1/2}, \qquad (4)$$

which is derived from the width of the subharmonic resonance tongue of the damped Mathieu equation (Landau & Lifshitz 1976) and the capillary dispersion relation $\omega_0^2 = (\sigma/\rho)k^2$. (The above expression is valid for small μ; owing to the shape of the subharmonic tongue, Δk for larger μ is $\frac{1}{3}(\rho/\sigma\omega)^{2/3}a$, i.e. proportional to $a \sim (1+\mu)$ and not $\mu^{1/2}$.)

Previous large-aspect-ratio experiments exhibit the effects of small Δk at low viscosity. The observation of Tufillaro, Ramshankar & Gollub (1989) that an 'order–disorder' transition was geometry-dependent even when L was 50 to 100 times the wavelength λ may be due to the fact that the quantitative values $\pi/L = 0.39$ cm^{-1} and $\Delta k \approx 0.45$ cm^{-1} (at $\mu = 0.07$) were similar. The experiments of Christiansen, Alstrom & Levinsen (1992) were also performed at parameters where $\Delta k \approx 0.65$ cm^{-1} (at $\mu = 0.08$) was near $\pi/L = 0.37$ cm^{-1} (where L is the diameter), and this may explain the observed aspect-ratio dependence of the resulting patterns.

The container can only be considered 'large' when $L \gg \pi/\Delta k$ so that as $\nu \to 0$, L should increase as $1/\nu$. In this feature the low-viscosity Faraday problem differs qualitatively from the Rayleigh–Bénard problem, which does not display such strong finite-size effects.

Figure 3 is a photograph of a single Bessel mode obtained with pure water. The observation of single modes of the container is very common at low viscosities even when the aspect ratio L/λ is large (cf. Douady & Fauve 1988).

To study the patterns that would be selected by nonlinearity in a horizontally infinite
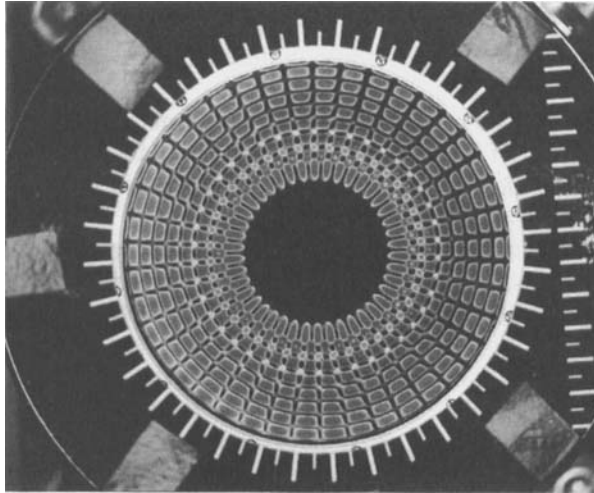
FIGURE 3. The influence of sidewall geometry at low viscosity. A single standing-wave Bessel mode J_{21} appears on the surface of water in a circular container of 12 cm diameter and depth 0.29 cm subjected to sinusoidal vertical vibration at 75 Hz.

system, and not by container shape and size, it is essential that $\Delta k \gg \pi/L$ so that finite-size effects can be safely neglected. By choosing fluids of higher viscosity, this condition is satisfied at smaller values of L and μ than are possible with low-viscosity fluids such as water.

Previous experiments have shown that finite-size effects are reduced at higher viscosity. Douady (1989, 1990) measured stability thresholds $a_c(\omega)$ in a 'one-dimensional' experiment (a vessel 6.5 cm × 1.6 cm) at forcing frequencies from 23 to 42 Hz, for water and for silicone oil (Rhodorsil 47V20 at 30 °C, $\nu \approx 0.18$ cm^2 s^{-1}, $\rho \approx$ 0.94 gm cm^{-3}, $\sigma \approx 20.5$ dyn cm^{-1}). In water, stability thresholds showed clearly the resonance tongues of individual modes of the container. For silicone oil the threshold was a much smoother function of frequency, although resonance tongues were still apparent.

The main qualitative results reported in the present article can be obtained with either silicone oil or glycerol/water mixtures. Quantitative measurements were made with a mixture of 88% (by weight) glycerol and 12% water, which has a kinematic viscosity $\nu \approx 1.00$ cm^2 s^{-1} at 23 °C.

A wider band Δk of unstable wavenumbers could also be achieved by increasing the forcing frequency ω, although at high frequencies it becomes mechanically difficult to achieve a clean vertical oscillation of the container that is free of horizontal and other motions. Furthermore, the stability threshold (again assuming low viscosity, infinite depth and capillary waves) is

$$a_c = 8(\rho/\sigma)^{1/3}\nu\omega^{5/3} \tag{5}$$

so that with a given maximum achievable acceleration (experiments are limited by the size of the vibration system) it is preferable to increase the product $\nu\omega \sim \Delta k$ by increasing ν rather than ω, since a_c grows only linearly with ν but as the $\frac{5}{3}$ power of ω.

2.3. *The infinite-depth limit and nearly marginal long-wavelength modes*

Theoretical studies of the Faraday instability often assume that the fluid depth is much larger than the pattern wavelength. In the infinite-depth limit the inviscid linear stability analysis is simplified because the velocity potential ψ is proportional to

$\exp(kz)$ rather than to a linear combination of $\exp(kz)$ and $\exp(-kz)$ as would be required to satisfy the impermeability condition $\partial_z \psi = 0$ on the bottom of the container.

However, in this limit there is no damping mechanism for long-wavelength modes. Therefore the reduction of the hydrodynamic problem to a set of amplitude equations for critical wavevectors $\{k_j\}$, $|k_j| = k_c$, cannot be justified in the infinite-size limit $L \to \infty$ because the longest-wavelength modes allowed by the container (i.e. $k = \pi/L \to 0$) have arbitrarily small decay rates $2\nu k^2$. They must then be considered marginal modes in the nonlinear analysis. Any nonlinear mechanism which transfers energy to a small wavevector k could destabilize that mode and destroy a pattern of critical wavevectors. Thus there is no finite range of the bifurcation parameter μ for which such amplitude equations are valid, because the small-wavevector modes cannot be considered 'slaved' to the critical wavevectors. This is another feature of the Faraday problem distinguishing it from the Rayleigh–Bénard problem, which has no nearly marginal long-wavelength modes. (Except with idealized 'free-slip' boundary conditions; see Zippelius & Siggia 1983. The problem does not arise near threshold for realistic boundary conditions, although coupling to long-wavelength modes becomes important at higher Rayleigh numbers.)

Patterns in large-depth Faraday experiments exhibit long-wavelength modulations which lead to spatial disorder and chaotic dynamics (Ezerskii *et al.* 1986). The major exceptions are square patterns observed in square or rectangular containers at low viscosity (Douady & Fauve 1988), where sidewalls help to stabilize the pattern due to the quantization effects previously discussed.

Incorporation of the marginal modes near $k = 0$ would complicate the nonlinear analysis. In the present series of experiments these modes are suppressed by choosing a fluid depth h which is of the same order as the pattern wavelength λ. Owing to the no-slip condition on the bottom of the container, there is a finite decay rate (due to finite shear) associated with all long-wavelength modes. (All modes involve horizontal velocity somewhere on the surface and thus between the surface and the bottom there is finite shear and thus finite energy dissipation, leading to a decay rate of order ν/h^2 in the long-wavelength limit.) The use of amplitude equations which ignore these modes is thus valid in some finite neighbourhood of the stability threshold for containers of arbitrarily large L. Experimentally we find that with such depths the patterns arising near the threshold are often stationary, defect-free and stable over relatively wide ranges of the forcing amplitude.

If the bottom is flat, then regardless of the depth the hydrodynamic problem retains the symmetries of the plane (ignoring sidewalls), so that the methods used in the nonlinear analysis and the form of the amplitude equations do not change. The critical eigenmodes have a more complicated spatial and temporal form, especially at high viscosity, but these can be computed numerically as will be described in a related publication (Tuckerman *et al.* 1994). Coefficients appearing in the amplitude equations can also be determined numerically or from experimental measurements.

2.4. *Amplitude equations for single-frequency forcing*

The forcing function $f(t)$ studied in all previous experiments is

$$f(t) = a \cos(2\omega t). \tag{6}$$

For low-viscosity fluids it is well established theoretically and experimentally that the critical standing-wave modes respond subharmonically, i.e. with frequency ω. (This is verified, by stroboscopic means, at the higher viscosities used in the present study.)

Consider a set of N standing-wave modes with critical wavevectors $\pm k_j$, $|k_j| = k_c$, $j = 1, \ldots, N$. The surface deformation can be written as

$$\zeta(x, t) = \hat{\zeta}(t) \sum_{j=1}^{N} A_j(t) \exp(ik_j \cdot x) + \text{c.c.} + \ldots, \tag{7}$$

where $\hat{\zeta}(t)$ is the temporal eigenfunction, which is real and has the subharmonic symmetry $\hat{\zeta}(t + \pi/\omega) = -\hat{\zeta}(t)$, i.e. its Floquet multiplier is -1 with respect to the period π/ω of the forcing. (In the low-viscosity limit $\hat{\zeta}(t)$ is sinusoidal. Without performing a Floquet analysis, we nonetheless anticipate that at finite viscosity the use of Floquet multipliers to describe the critical eigenmodes will be appropriate even though the temporal response is not necessarily purely sinusoidal.) The complex amplitudes A_j are assumed to vary slowly in time. Amplitude equations up to cubic order will have the form (ignoring spatial derivatives)

$$\tau_0 \partial_t A_j = \mu A_j - \sum_{l=1}^{N} \beta(\theta_{lj}) |A_l|^2 A_j, \quad j = 1, \ldots, N, \tag{8}$$

where θ_{lj} is the angle between k_l and k_j. The value of τ_0 for the low-viscosity theory is $1/(2\nu k_c^2)$. Hereafter t is rescaled such that $\tau_0 = 1$. The self-interaction coefficient $\beta(0)$ is assumed to be positive and the amplitudes are rescaled such that $\beta(0) = 1$.

In general, and especially for large L, the amplitudes can also be slowly varying functions of the horizontal space coordinates, and (8) will have terms involving horizontal amplitude gradients, as for example in the complex Ginzburg–Landau and nonlinear Schrödinger equations. Slow space-dependence of the complex amplitudes permits analysis of phenomena such as defects and domain walls. In the present paper we restrict our attention to the problem of pattern selection, and thus we consider only homogeneous patterns.

The absence of quadratic terms in (8) results from the subharmonic symmetry. Because $\hat{\zeta}(t)$ changes sign during each forcing period, the amplitude equations must be sign invariant, since they involve a timescale much larger than the basic period. The mechanism which favours hexagons in non-Boussinesq convection (Palm 1960), involving small quadratic terms, is thus not available in this case.

This system of amplitude equations has been studied by many authors (cf. Malomed, Nepomnyaschiĭ & Tribelskiĭ 1989; Newell & Pomeau 1993; Müller 1993a). It is of gradient form $\partial_t A_j = -\partial \mathscr{F}/\partial A_j^*$, with Lyapunov function

$$\mathscr{F} = -\mu \sum_{j=1}^{N} |A_j|^2 + \frac{1}{2} \sum_{j=1}^{N} \sum_{l=1}^{N} \beta(\theta_{lj}) |A_l|^2 |A_j|^2. \tag{9}$$

Stable symmetric $2N$-fold patterns of any N are possible, depending on the cubic coupling function $\beta(\theta)$. The value N which minimizes the arithmetic average $(1/N) \sum_{l=1}^{N} \beta(l\pi/N)$ has the deepest minimum of $\mathscr{F}$ and is thus selected. It bifurcates supercritically from the flat surface and each A_j has an arbitrary spatial phase. (This is true only at cubic order. Certain phase relations are determined by higher-order terms; cf. Golubitsky, Swift & Knobloch 1984.)

In the Faraday problem $\beta(\theta)$ can be strongly influenced by nonlinear interactions with wavenumbers other than k_c. Milner (1991) encountered such an effect which led, in his formulation of the small-viscosity nonlinear analysis, to a divergence of $\beta(\theta)$ for $\theta = 74.9°$. In the usual capillary infinite-depth limits, where $\omega_0^2(k) = (\sigma/\rho) k^3$, this involves an interaction with the harmonic response $\omega_0(|k_j + k_l|) = 2\omega = 2\omega_0(k_c)$ for

$2\cos(\theta/2) = 2^{2/3}$ as shown in figure 4. The divergence is toward $+\infty$, so that the system tries to avoid pairs of critical wavevectors separated by 74.9°.

To see the effect of the second wavenumber, note that in figure 4 the interactions among A_j, A_l, A_l^* and B can be described by the equations

$$\partial_t B = -\epsilon B + A_l A_j + \ldots, \tag{10}$$

$$\partial_t A_j = \mu A_j - A_l^* B + \ldots, \tag{11}$$

where ϵ is a small decay rate for B and the quadratic interaction coefficients have been set to ± 1 by appropriate amplitude scalings. The signs are consistent with conservation of energy $\sim |A_j|^2 + |B|^2$ in the unforced inviscid case where $\mu = \epsilon = 0$. When $\epsilon \gg \mu > 0$, B will be slaved to the A modes and can be replaced in (11) by the steady-state solution $B = A_l A_j/\epsilon$ of (10), giving

$$\partial_t A_j = \mu A_j - \frac{1}{\epsilon}|A_l|^2 A_j. \tag{12}$$

Thus $\beta(\theta_{lj})$ diverges as $1/\epsilon$ when $\epsilon \to 0$. Milner considered damping only for the A modes, so that ϵ was zero. (Physically, the harmonic mode B is also damped by viscosity, but Milner did not take this into account.) With finite viscosity ϵ is non-zero and the resonance at B is not perfectly sharp, so that nearby wavevectors can also influence $\beta(\theta)$ at nearby angles.

Milner's calculation of $\beta(\theta)$ directly from the hydrodynamic equations allowed him to compute $\mathscr{F}$ for $N = 1, 2, 3$ (parallel lines, squares and hexagons). He found that squares were the preferred pattern.

2.5. *Arbitrariness of the forcing function*

There is no experimental restriction on the choice of forcing function $f(t)$. Early experiments such as Faraday's used mechanical vibration and thus sinusoidal forcing was a convenient choice. Modern experiments use electromagnetic vibration exciters, and any electronically generated waveform can be used.

Because the forcing acceleration is always vertical, the symmetries of the (horizontal) plane are retained in the linear and nonlinear problems for the primary instability from the flat surface, regardless of the choice of $f(t)$. An intriguing aspect of the Faraday instability is that with two frequencies there exist codimension-2 bifurcations with two simultaneously critical wavenumbers k_{1c} and k_{2c}. By rotational invariance each critical wavenumber implies a circle of critical wavevectors. Nonlinear interactions between wavevectors on the two circles can strongly influence $\beta(\theta)$ when $2\cos(\theta/2) \approx k_{2c}/k_{1c}$ (cf. Newell & Pomeau 1993), and this in turn affects the selection of the asymptotic pattern.

The dispersion relation (2) provides an estimate of the frequency ratio needed to produce a desired wavenumber ratio. However, the linear stability problem is not insensitive to the superposition of frequencies, so that the two wavenumbers at bicriticality are not exactly the individual frequencies (Tuckerman *et al.* 1994). Furthermore, in the nonlinear regime a finite band of wavenumbers is unstable around each critical k and thus the ratio k_{2c}/k_{1c} is not precisely fixed.

The present experimental study is restricted to pairs of frequencies in the ratios of small integers. (If the two frequencies are incommensurate, $f(t)$ is quasi-periodic and no Floquet analysis can be used in the linear problem.) The forcing functions are of the form

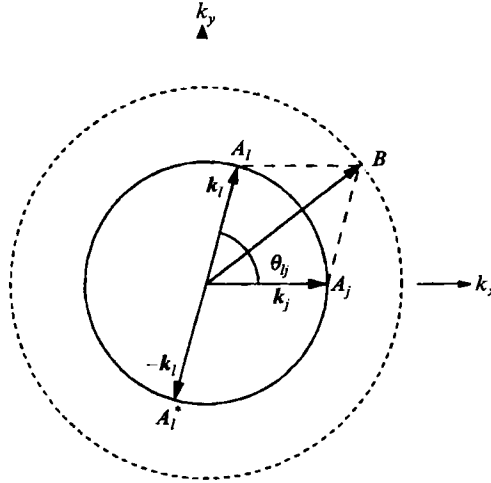$$f(t) = a[\cos(\chi)\cos(m\omega t) + \sin(\chi)\cos(n\omega t + \phi)] \tag{13}$$

FIGURE 4. Influence of the harmonic resonance on the cubic coefficient $\beta(\theta_{ij})$. For low-viscosity capillary waves, the mode B will resonate spatially and temporally with the quadratic interaction of A_j and A_l when θ_{ij} is such that $|k_j + k_l| = 2\cos(\theta_{ij}/2)k_c = 2^{2/3}k_c$, corresponding to the harmonic response tongue of figure 2. The temporal Floquet multiplier is -1 for the subharmonic modes A_j, A_l, and $+1$ for the harmonic mode B. If B is slightly damped, it can be slaved to the A modes at quadratic order, but at cubic order it will strongly affect $\beta(\theta)$ at the angle $\theta = 74.9°$.

with m and n relatively prime (by choice of ω). The angle χ serves to mix the two amplitudes. The phase of $m\omega t$ is zero by choice of the time origin, and the other phase can be chosen within $0 \leqslant \phi < 2\pi/m$ because (13) is invariant with respect to $\phi \to \phi + 2\pi/m$, $t \to t + 2p\pi/m\omega$ for some integer p. The experimental protocol is to fix the parameters m, n, ω, ϕ and χ and to increase a slowly, starting from the stable flat surface, to traverse the stability threshold.

2.6. *Amplitude equations for even/odd forcing*

For single-frequency forcing the exclusion of quadratic terms in the amplitude equations is due to the subharmonic symmetry. With two-frequency forcing, quadratic terms can arise. Consider for example the case $m = 2$, $n = 1$. When $\chi = 0$ this corresponds to simple sinusoidal forcing $f(t) = a\cos(2\omega t)$ and the critical mode will then have a subharmonic response with $\hat{\zeta}(t + \pi/\omega) = -\hat{\zeta}(t)$. In this case, sign invariance of the amplitude equations results from the fact that *there exists a period π/ω for which the forcing function is exactly periodic and over which the critical eigenmodes change sign.*

For χ non-zero and small, the critical eigenmode and its stability threshold are perturbed. However, no exact subharmonic symmetry remains because $f(t)$ is periodic only over the longer period $2\pi/\omega$ and not with period π/ω. Over the longer period $\hat{\zeta}(t)$ does not change sign. Thus *there exists no period for which $f(t)$ is exactly periodic and over which the critical eigenmodes change sign*, and therefore quadratic terms are no longer prohibited in the amplitude equations.

The above argument for $m = 2$ and $n = 1$ can be generalized. Whenever an even frequency is perturbed by an odd frequeny (m and n are relatively prime), small quadratic terms will in general be present. When both frequencies are odd, or when an odd frequency is perturbed by an even frequency, the critical modes always change sign over one period of the forcing and thus quadratic terms are prohibited.

The presence of quadratic terms applies only to triad interactions with wavevectors

forming equilateral triangles. Thus if N is a multiple of 3 and $\theta_{j,j+N/3} = 2\pi/3$, the amplitude equations (8) become

$$\partial_t A_j = \mu A_j + \alpha A^*_{j+N/3} A^*_{j-N/3} - \sum_{l=1}^{N} \beta(\theta_{lj}) |A_l|^2 A_j, \quad j = 1,\ldots,N, \tag{14}$$

where $A_{j\pm N} \equiv A_j$ for all j. The system (14) is again of gradient form, having the Lyapunov function

$$\mathscr{F} = -\mu \sum_{j=1}^{N} |A_j|^2 + \frac{\alpha}{3} \sum_{j=1}^{N} (A_j A_{j+N/3} A_{j-N/3} + A^*_j A^*_{j+N/3} A^*_{j-N/3})$$

$$+ \frac{1}{2} \sum_{j=1}^{N} \sum_{l=1}^{N} \beta(\theta_{lj}) |A_l|^2 |A_j|^2. \tag{15}$$

In the low-viscosity limit, the quadratic coefficient α is to leading order proportional to the perturbation amplitude $a \sin \chi$, for the case $m = 2$, $n = 1$. (For $m = 4$, $n = 5$, α is proportional to $[a \sin \chi]^2$; the exponent is determined by a perturbation analysis of the Mathieu equation.) Furthermore, it can be shown that there exists a phase $\phi = \phi_0$ at which $\alpha = 0$, by noting that $\phi \to \phi + \pi$ is equivalent to $\chi \to -\chi$ and thus $\alpha \to -\alpha$; therefore the real-valued function $\alpha(\phi)$ must have a zero.

The case $N = 3$ recalls the theory of hexagons in non-Boussinesq convection (Palm 1960). Stable hexagons are predicted in a neighbourhood of $\mu = 0$. (See Ciliberto *et al.* 1990 or Pampaloni *et al.* 1992 for recent experimental results concerning hexagons and the hexagon/roll transition.)

The case $N = 6$ includes the possibility of twelvefold quasi-patterns, in addition to lines, hexagons and squares. This was considered by Malomed *et al.* (1989), who concluded that twelvefold quasi-patterns could be stable within this model, for some finite parameter ranges.

2.7. *Summary of theoretical motivations*

The theoretical motivations for the present experimental study are as follows. First, it appears that the problems posed by the low-viscosity and infinite-depth limits can be avoided and that the fluid depth and viscosity can be chosen such that selected patterns are amenable to theoretical analysis on the basis of cubic-order amplitude equations for finite critical wavevectors, ignoring both long-wavelength modes and finite-size effects. Secondly, the deliberate breaking of the subharmonic symmetry with an even/odd pair of frequencies introduces quadratic terms into the amplitude equations whose coefficient α is proportional to the amplitude of the perturbing (odd) frequency. Thirdly, the cubic-order coupling function $\beta(\theta)$ may be strongly influenced by the presence of a second critical wavenumber, and by adjusting the amplitudes of two forcing frequencies, wavenumber bicriticality may be achieved. Even in this bicritical situation, where neither forcing amplitude can be considered small, the strength of the quadratic terms can still be controlled through the dependence of α on the phase ϕ of the odd frequency. The parameters which are most interesting from the point of view of their effect on the nonlinear coefficients in the amplitude equations, namely, n, m, χ and ϕ for the two-frequency forcing $f(t)$, are easily adjusted since they enter the experiment electronically as part of the waveform generation of $f(t)$. Thus the two-frequency Faraday experiment is a convenient way to study certain fundamental issues in pattern formation.

Although much of our discussion has made use of results from single-frequency small-viscosity infinite-depth theory, we do not expect that these results will be directly

applicable to the current series of experiments. Coefficients appearing in the amplitude equations will be affected by viscosity, depth and multiple-frequency forcing.

3. Experimental apparatus

The experimental apparatus consists of a cylindrical container fixed rigidly to the armature of a vibration exciter. The container is filled to its brim with a layer of fluid. The vibration exciter, which is solidly anchored, oscillates the container vertically according to a computer-generated waveform. The resulting standing-wave pattern is visualized by reflected light from an axisymmetric light ring centred above the container, and images are captured by a video or film camera mounted on axis, looking down.

3.1. *Containers*

The container used for quantitative measurements is a cylinder with diameter $L = 12$ cm and depth $h = 0.29$ cm. Pattern wavelengths range from 0.6 to 0.9 cm. Roughness of the bottom must be small compared to the depth and the bottom must be level. The bottom is black Formica, which when laminated to a rigid aluminium support is flat to within ± 0.003 cm. Sidewalls are aluminium. The empty container with mounting hardware and accelerometer weighs 255 gm.

The brimfull technique of Benjamin & Scott (1979) and Douady (1989) is used as shown in figure 5. The fluid surface is pinned at a discontinuity of the slope of the sidewall. This corner is machined to a fixed height $h = 0.29$ cm relative to the bottom. When the fluid is introduced and the surface attaches itself to the corner, adjustments are made to the fluid volume and the levelling of the apparatus such that the resulting surface is precisely flat and thus there is no meniscus. This is done by viewing the reflected images of laboratory objects or walls; the flat surface becomes a non-distorting mirror only when the volume is correct and the apparatus is level. The brimfull technique provides a homogeneous Dirichlet condition on the surface height, and it facilitates accurate filling and levelling. The precisely flat surface is also an exact trivial solution of the hydrodynamic problem in the presence of vertical forcing and thus meniscus waves are not produced.

A variety of other containers is used to verify that patterns do not depend on container shape. Several of these are milled from solid aluminium and then spray-painted black, with depths from 3 to 5 mm. They include square, hexagonal and octagonal geometries and one container whose sidewalls follow the irregular outline of a map of France. Horizontal dimensions of these containers range from 5 to 8 cm.

3.2. *Fluids*

All quantitative results presented in this article were obtained with a mixture of 88% (by weight) glycerol and 12% distilled water, which has density $\rho = 1.22$ g cm^{-2}, kinematic viscosity $\nu = 1.00$ cm^2 s^{-1} (at 23 °C), and surface tension $\sigma = 65$ dyn cm^{-1}. The fluid is prepared in batches of 250 ml on an electronic balance and mixed with a magnetic stirrer to prevent entrainment of air. The mixtures are stored in sealed bottles to prevent evaporation of water.

Approximately 33 ml of fluid is required to fill the cylindrical container. A non-vibrating glass and Plexiglas cover, which forms a seal with the housing of the vibration exciter, isolates the fluid with a volume of air, approximately 2 l, with which it equilibrates after a small gain or loss of water.
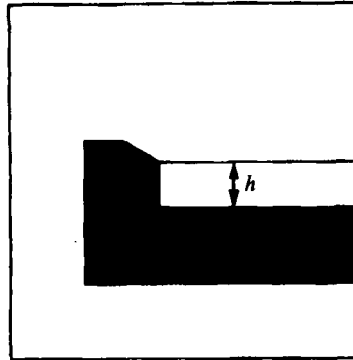
FIGURE 5. Sidewall boundary condition. The aluminium sidewall has a corner where the slope changes discontinuously from 90° to 30°. With a glycerol/water mixture the contact line becomes pinned at the corner, making possible the preparation of a flat surface with no meniscus. The 30° 'beach' makes the fluid fall back into place if the contact line is temporarily disrupted.

3.3. *Mechanical system*

The use of high-viscosity fluids leads to high critical acceleration a_c, which necessitates a mechanically simple design. Containers are attached rigidly to the armature of an electromagnetic vibration exciter (Bruel & Kjaer model 4808). The housing of the vibrator is bolted to reinforcing steel which is embedded in a cement block of size $(30 \text{ cm})^3$. The cement is contiguous with a structural beam of the laboratory building. The moving parts of the vibration exciter weigh 160 gm. It produces a maximum instantaneous force of 112 N.

The internal design of the vibration exciter uses sheet metal and rubber radial supports for the moving armature. This system cannot eliminate all horizontal motions. To minimize horizontal motions the cylindrical container is symmetrically fabricated so that its centre of mass coincides with its axis and thus the axis of the vibration exciter. The accelerometer, which is mounted off-axis, is counterbalanced. Horizontal components of acceleration are measured from time to time by mounting the accelerometer horizontally. Such components are typically less than 3% of the vertical acceleration.

Mechanical modes of the vibration exciter lead to frequency-dependent amplitude and phase errors in its response to the driving signal. These are compensated electronically as described below. Such mechanical modes could in principle lead to horizontal and other motions which would influence the observed pattern. However, the qualitative results are unchanged when another model of vibrator (B & K 4809) is substituted.

To obtain homogeneous patterns it is often necessary to add small weights to the edges of the container to tune the mechanical behaviour of the vibrator. Weights between 0.2 and 6 g are placed such that the resulting pattern near the stability threshold exhibits homogeneous amplitude over the area of the surface. Without such weights the pattern typically arrives first on one side of the container.

3.4. *Waveform generation, data acquisition and control*

The generated signal $f^{(g)}(t)$ which controls the vibration exciter is produced digitally in real time by a small computer (IBM AT). The program updates this signal 8000 times per second by computing

$$f^{(g)}(t) = a^{(g)}[\cos{(\chi^{(g)})}\cos{(m\omega t + \phi_m^{(g)})} + \sin{(\chi^{(g)})}\cos{(n\omega t + \phi_n^{(g)})}] \qquad (16)$$

with 15-bit integer arithmetic. A National Instruments AT-MIO-16F-5 multifunction I/O board performs 12-bit conversion to an analog signal which is then low-pass filtered (cutoff 500 Hz) to remove the 8 kHz component. A B & K 2712 power amplifier drives the vibration exciter.

Vertical acceleration is measured by a B & K 4393 piezoelectric accelerometer and a B & K 2635 calibrated charge amplifier. The signal is converted by the AT-MIO-16F-5 to a 12-bit value which is examined by the program that generates the original signal. With respect to the same time origin, the measured signal $f^{(m)}(t)$ is processed according to the ansatz

$$f^{(m)}(t) = a_m^{(m)} \cos{(m\omega t + \phi_m^{(m)})} + a_n^{(m)} \cos{(n\omega t + \phi_n^{(m)})} + r(t), \qquad (17)$$

where $r(t)$ is a residual. The measured amplitudes $a_m^{(m)}$, $a_n^{(m)}$ and phases $\phi_m^{(m)}$, $\phi_m^{(m)}$ are determined by real-time numerical integration of the equations

$$r(t) = f^{(m)}(t) - a_m^{(m)} \cos{(m\omega t + \phi_m^{(m)})} - a_n^{(m)} \cos{(n\omega t + \phi_n^{(m)})}, \qquad (18)$$

$$\tau \, \partial_t a_j^{(m)} = r(t) \cos{(j\omega t + \phi_j^{(m)})}, \quad j = n, m, \qquad (19)$$

$$\tau \, \partial_t \phi_j^{(m)} = -r(t) \sin{(j\omega t + \phi_j^{(m)})}, \quad j = n, m. \qquad (20)$$

This constitutes a two-frequency lock-in technique for known frequencies, which obtains phase information relative to a common time origin. The time constant τ is typically set to 3 s. RMS residuals $\langle r(t) \rangle^{1/2}$ are 3 % or less of the measured amplitudes. For efficiency all cosines and sines are found by 12-bit table lookups. Timesteps for (19), (20) are $1/4000$ s.

The phase $\phi_m^{(m)}$ is made zero (which corresponds to setting the overall time origin) by control of the generated phase $\phi_m^{(g)}$, i.e. by integrating

$$\tau \, \partial_t \phi_m^{(g)} = -\phi_m^{(m)}. \qquad (21)$$

The phase $\phi_n^{(m)}$ is made equal to the desired parameter value ϕ by control of $\phi_n^{(g)}$, i.e. by integrating

$$\tau \, \partial_t \phi_n^{(g)} = \phi - \phi_n^{(m)}. \qquad (22)$$

Data taking is performed with automatic ramping of the generated $a^{(g)}$ at 1 % per minute for fixed $\chi^{(g)}$. At transition boundaries ramping is halted for 10 s or more to obtain asymptotic values from the integration of the lock-in equations (19). The measured amplitudes are recorded separately; χ is not directly measured or controlled but is determined by $\chi^{(m)} = \tan^{-1}(a_n^{(m)}/a_m^{(m)})$.

3.5. *Visualization*

Patterns are visualized by light reflected from the fluid surface. A video or 35 mm film camera looks directly down on the surface from a distance of from 128 to 165 cm. The light source is axisymmetric, so that the visualization introduces no preferred horizontal direction. (This isotropy is important for the recognition of the twelvefold quasi-pattern, which in ordinary room light appears to be disordered.) An array of 30 incandescent 15 W lamps is mounted symmetrically on a circle of radius 14.5 cm. To eliminate the thirtyfold symmetry this light is passed through an axisymmetric translucent plastic diffuser in the form of an annulus of inner radius 14 cm and outer radius 18 cm. The lamps and annular diffuser surround the camera. Black limiters are used to suppress unwanted reflections. The camera lens is mounted in a light baffle. The flat surface appears black since 14 cm is more than twice the container radius and thus there is no reflection from the diffuser to the camera. Light transmitted through the surface is absorbed by the black bottom of the container.

Since the distance to the camera is large compared to the container radius, radial

effects are small. From a point on the surface, a reflection will reach the camera when the surface gradient is between 2.4° and 3.1° from horizontal (for camera distance 165 cm). These angles are small compared to the maximum gradients in the patterns under study, which often exceed 45°. In photographs, where exposure times are typically 1 s or more, many times the period of the standing waves, white corresponds to points whose time-averaged gradient norm is small but non-zero, for example very close to a point of maximum deformation. Nodal lines do not have small average gradient norm and thus are not distinguished. White line segments in photographs correspond to lines of small surface gradient where surface curvature (transverse to the line) is oscillating.

The video camera allows stroboscopic exposure of the CCD array. The triggering pulse originates in the computer and is synchronized with the forcing function $f(t)$. The stroboscopic video camera, or an ordinary stroboscope, is used to study the surface in slow motion and to determine the response period and thus the Floquet multiplier of each pattern.

The shadowgraph technique is not used as this requires the placement of a lamp or mirror between the container and the vibration exciter, and thus a supporting structure for the container. Such a support complicates the mechanical system and increases the vibrating mass. The maximum achievable acceleration would be reduced, given a specified maximum force. Shadowgraphs in surface-wave experiments do not provide an approximately linear response (as can be obtained for Rayleigh–Bénard convection). Light passing through a deformed surface is strongly deflected due to the abrupt change in the index of refraction. Both visualization techniques, shadowgraph and reflection, are therefore strongly nonlinear. The reflection method is more convenient since it separates the visualization from the mechanical system.

3.6. Temperature control

Glycerol/water mixtures have temperature-dependent viscosity. For an 88% mixture, temperature control to within ±0.1 K is needed in order to achieve stability thresholds that are reproducible to within ±1%. This is accomplished with a two-stage temperature control system consisting of a water bath and low-intensity infrared light.

The main source of heat arriving at the container is the coil of the vibration exciter. About 2 W, which is a small fraction of the power dissipated in the coil, arrives at the fluid through the container and its mounting hardware. This is roughly compensated by cooling the outside of the stationary glass and Plexiglas cover to 10 °C, so that the air inside the cover is cooler than the fluid with which it is in contact.

Two thermistors (Dale 1T5001-3) are flush-mounted in the container sidewall, diametrically opposed, in contact with the fluid. One thermistor is used to control the temperature while the other allows an estimation of horizontal temperature gradients. The control thermistor is part of a bridge circuit. The analog signal from the bridge is converted by the AT-MIO-16F-5 and examined by proportional-differential control software. A relay circuit and an asynchronous D.C. motor coupled to a thyristor (commercial 'dimmer switch') varies the intensity of four reflector bulbs placed approximately 50 cm above the container, outside the glass and Plexiglas cover and away from the vertical line of sight of the camera. The bulbs are connected in series to reduce their operating temperature and thus decrease the ratio of visible to infrared light. The light is absorbed by the black bottom of the container, thus heating the fluid.

This two-stage temperature control system results in a small vertical gradient since cooling is accomplished through the fluid surface, i.e. through the air, while heating is done via the black bottom of the container.

4. Results with single-frequency forcing

4.1. *Squares versus lines*

Using glycerol/water mixtures of varying viscosity, it is found that squares are the preferred pattern below $v \approx 0.7 \, \text{cm}^2 \, \text{s}^{-1}$. For larger viscosities the pattern changes to parallel lines as shown in figure 6. The measured dispersion relation is shown in figure 7. The agreement with inviscid theory is good at low frequencies. At higher frequencies dissipation becomes more important; its effect is to reduce the critical wavenumber.

4.2. *Lines, defects, circles and spirals*

The behaviour of the lines is similar to that of rolls in convection experiments. In particular, they prefer to be aligned normal to the sidewalls, especially at higher forcing amplitudes. The result in a circular geometry is a bowed pattern. The wavelength near the centre is smaller than near the circumference, and as the forcing amplitude is increased this can lead to spontaneous defect-pair generation as in figure 8; similar behaviour in convective rolls at low Prandtl number was studied by Croquette (1989*a*, *b*). The defects migrate outward and are eventually destroyed near the boundary; another defect pair is then produced.

The usual protocol for these experiments is to increase the forcing amplitude *a* slowly (about 1% per minute) to traverse the stability threshold starting from the stable flat surface. If instead the threshold is crossed by abruptly increasing *a*, patterns of circles or spirals appear, as in figures 9 and 10. The spiral pattern rotates with a period of about one minute. Different experimental runs produce circles or spirals at random. Similar effects are also observed in convective patterns (Croquette 1989; Bodenschatz *et al.* 1991).

4.3. *Discussion*

In many low-viscosity experiments a square pattern is observed at or near the primary transition. However, when $v \to 0$ the container size and shape can strongly influence the pattern due to the vanishing of the band of unstable wavenumbers. Thus square patterns observed in square or rectangular containers are not conclusive evidence of the preferred pattern for the infinite plane. Douady & Fauve (1988), for example, working with water, observed patterns that were identifiable as the modes $\sin(m\pi x/L)$ $\sin(n\pi y/L)$ of the square container, with m and n as high as 18, or as superpositions of such modes. Tufillaro *et al.* (1989), working with butanol at higher frequencies, also observed square patterns in a square container, but Δk was comparable to π/L. Thus it seems likely that the container geometry had some influence on the pattern, even though the squares were not aligned with the boundaries. Measurable boundary effects persist well into the chaotic regime, as recently reported by Gluckman *et al.* (1993). However, the published evidence generally indicates squares at low viscosity.

Previously, lines have been observed only in the experiments of Fauve *et al.* (1992) in CO_2 very close to the liquid–vapour critical temperature. In both glycerol/water and CO_2 the effects of viscous dissipation may be important; near a liquid–vapour critical point the viscosity remains finite while the density difference and the surface tension vanish, and the observed pattern wavenumber approaches a finite viscous-cutoff value. Large viscous dissipation means that these experiments (glycerol/water and CO_2) cannot be compared to existing low-viscosity theories; at the time of writing there is no satisfactory explanation for these patterns of lines. It may be speculated that high dissipation changes the geometry of figure 4 by preferentially reducing the wavenumber of the harmonic response at *B*. This would cause θ_{ij} to approach $\pi/2$ so that squares would be suppressed as the system tries to avoid wavevectors separated by this angle.
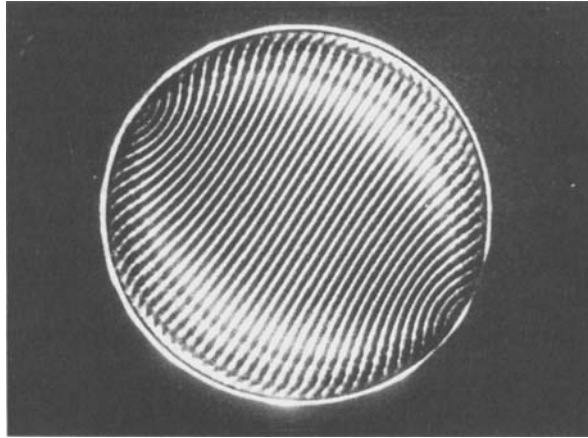
FIGURE 6. Single-frequency forcing at high viscosity. A pattern of essentially parallel lines is observed with a mixture of 88% glycerol and 12% water, having $\nu \approx 1.00$ cm^2 s^{-1}. The forcing frequency $2\omega/2\pi$ is 80 Hz.

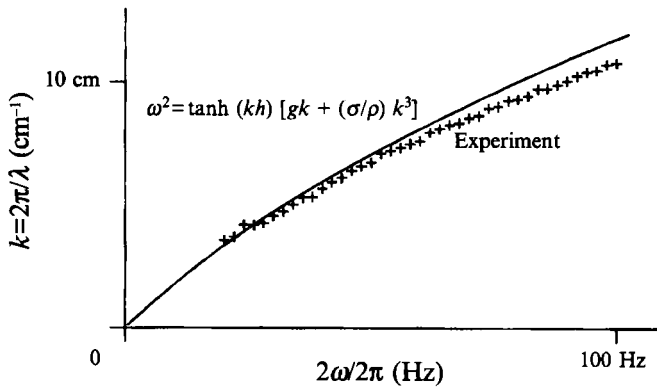FIGURE 7. Measured dispersion relation (crosses) for lines at viscosity $\nu = 1.00 \pm 0.05$ cm^2 s^{-1} is close to the theoretical zero-viscosity result (solid line). The values $\sigma = 65$ dyn cm^{-1} and $\rho = 1.22$ g m^{-3} for the theoretical curve are literature values for the glycerol/water mixture.
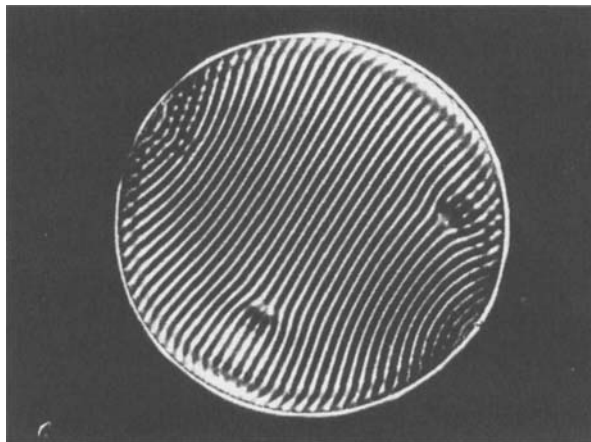
FIGURE 8. Defect-pair generation in a circular container. The fluid and forcing frequency are the same as for figure 6, with slightly higher forcing amplitude. Defect pairs are spontaneously produced near the centre and propagate outward.
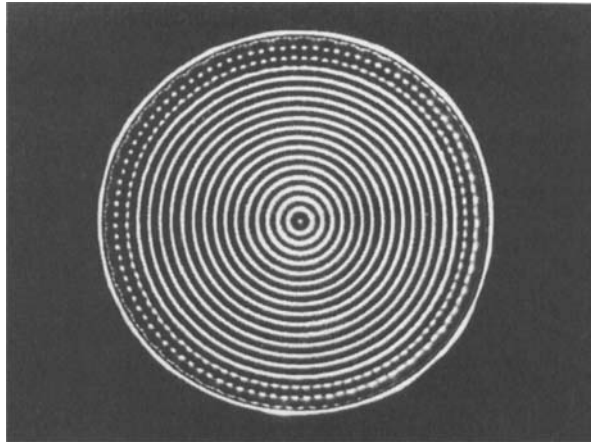
FIGURE 9. Circular pattern after abrupt transition. The flat surface becomes unstable after a rapid increase in the forcing acceleration a, giving rise to circular waves. The pattern is a result of the circular sidewall. Once created, it persists indefinitely.
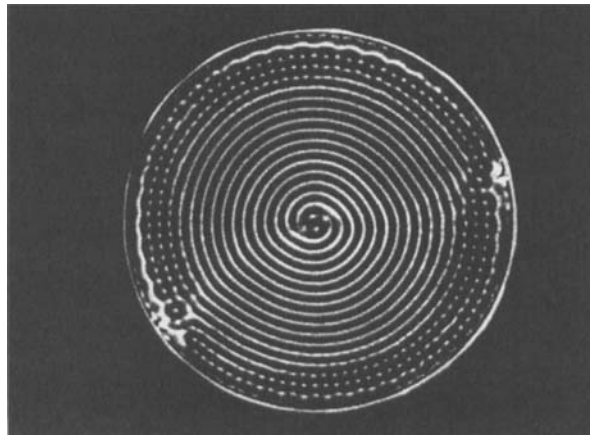
FIGURE 10. Spiral pattern after abrupt transition. Different experimental runs produce circles or spirals, apparently at random. The double spiral includes two defects at the boundary. The pattern rotates counterclockwise with a period of about one minute.

Although these patterns are similar to those observed in steady Rayleigh–Bénard convection, the timescales here are much shorter. Patterns develop in a few seconds and the dynamics of defects and long-range correlations involve times of the order of one minute.

5. Results with two-frequency forcing

5.1. *Lines and hexagons*

The case $m = 4$ and $n = 5$, for $\omega/2\pi = 14.6$ Hz, has been systematically investigated. Figure 11 shows the patterns arising at the primary instability for all values of χ and ϕ. Hexagons are apparent over much of the parameter domain. Figure 12 is the phase diagram for $\phi = 75°$.

The patterns indicated in these figures are the first ordered patterns observed after the flat surface loses stability. Very near the stability threshold, for μ slightly positive, the pattern is disordered or is clearly related to the geometry of the container. An
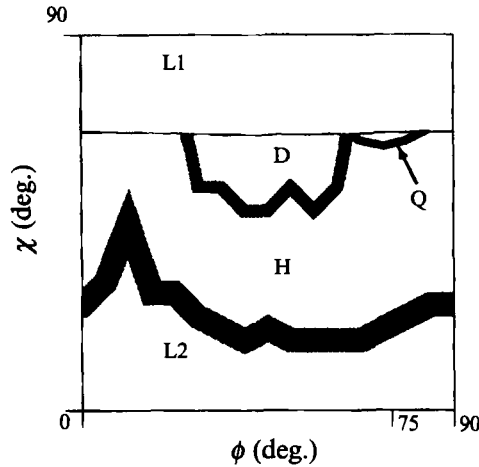
FIGURE 11. Patterns arising near the primary instability. For each point in this plane, i.e. for fixed ϕ and χ of the vertical acceleration $f(t) = a[\cos(\chi)\cos(4\omega t) + \sin(\chi)\cos(5\omega t + \phi)]$ with $\omega/2\pi = 14.6$ Hz, instability of the flat surface is obtained by slowly increasing the amplitude a. This figure shows which pattern is observed just above the primary transition from the flat surface: L1, lines with $k \approx 8.8$ cm^{-1}; Q, twelvefold quasi-pattern; H, hexagons; L2, lines with $k \approx 7.5$ cm^{-1}; D, dynamic states including breaking of the surface. The quasi-pattern is found only very near the bicriticality (the horizontal line) for ϕ near 75°. The figure is compiled from observations on a 16 × 17 grid of (ϕ, χ) values. Thick grey lines indicate regions where two patterns are in competition or are simultaneously present near the primary transition.
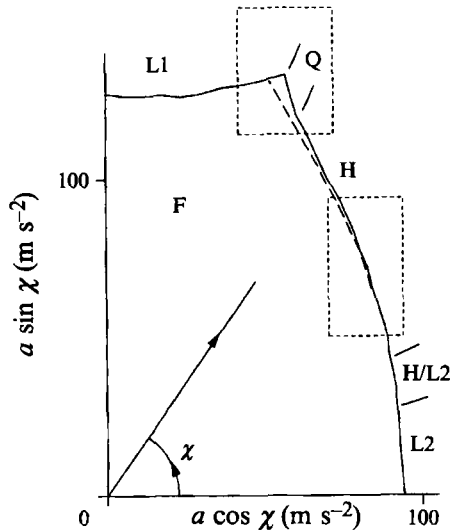
FIGURE 12. Stability boundaries for $\phi = 75°$ in the (a, χ)-plane, showing the primary transition from the flat surface (solid line), hysteresis (dashed line), and the pattern which develops just above $a = a_c(\chi)$. The instability is produced by fixing χ and increasing a as shown by the arrow. Dashed boxes correspond to figures 14 and 16.

ordered pattern is observed only when the nonlinear effects which select the pattern are strong enough to compete with boundary effects and inhomogeneities. When $\mu > 0.01$, an ordered pattern is usually observed.

For small χ, hexagons are not observed at the primary instability. The minimum value of χ necessary to produce hexagons is a function of ϕ as shown by the grey band
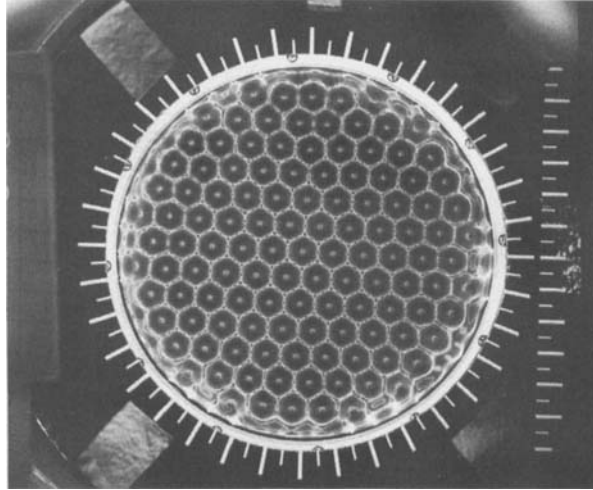
FIGURE 13. Hexagons produced by two-frequency forcing. The forcing acceleration is $f(t) = a[\cos(\chi)\cos(4\omega t) + \sin(\chi)\cos(5\omega t + \phi)]$, where $\omega/2\pi = 14.6$ Hz, $\phi = 75°$ and $\chi = 45°$. The pattern is observed at the primary transition from the flat surface.
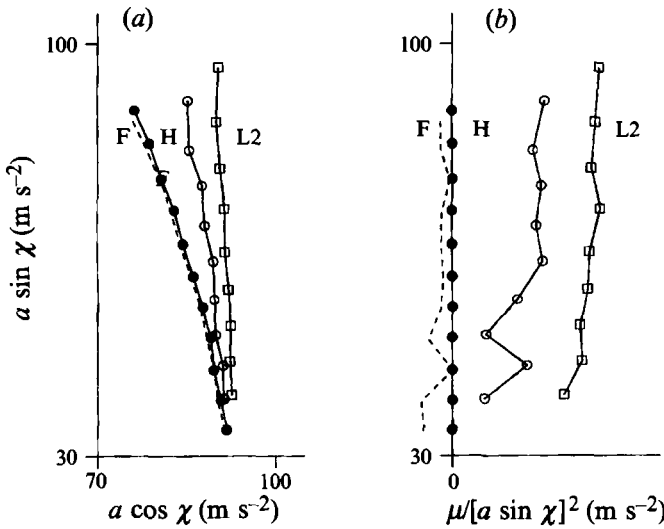

FIGURE 14. Hexagons-to-lines transition. In (a), the phase diagram is plotted in the plane of the two forcing amplitudes, and in (b) the same data are shown but with the horizontal axis $\mu/[a\sin\chi]^2$, where $\mu \equiv (a - a_c)/a_c$. Solid circles show the transition from the flat surface F to hexagons H as μ is slowly increased. Dashed lines show the transition from H to F for decreasing μ. Open circles and squares delimit the region in which the hexagon-to-lines transition takes place; squares show the final disappearance of hexagons as μ is increased, while circles show the final disappearance of lines as μ is decreased. The width of the region of stable hexagons is approximately proportional to the square of the amplitude $a\sin\chi$, as shown by the nearly vertical transition boundary in (b), especially in the upper portion of the diagram where the width is much larger than parameter fluctuations due to temperature.

in figure 11. Near $\phi \approx 15°$ clear evidence of hexagons is not observed until χ is 45° or more, whereas for other values of ϕ hexagons are more easily produced.

Figure 13 is a photograph of hexagons for $\phi = 75°$ and $\chi = 45°$. Figure 14 shows measurements of the transitions among the flat surface, hexagons and lines. The
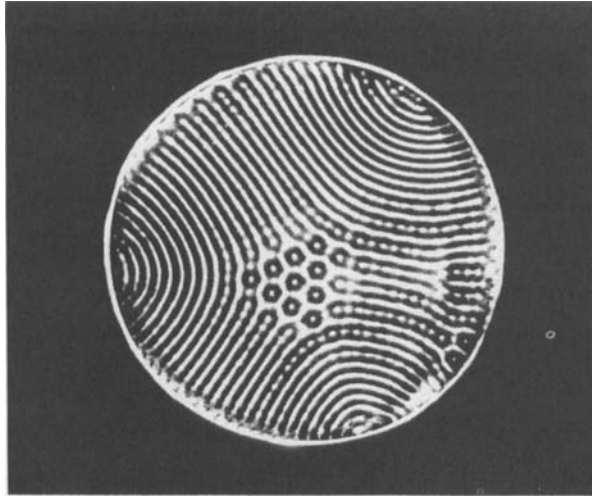
FIGURE 15. Hexagons-to-lines transition takes place over a finite range of μ where the two patterns coexist.
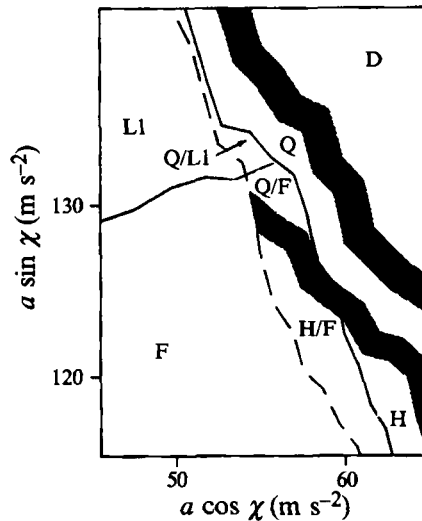

FIGURE 16. Transitions among the flat surface F, quasi-pattern Q, hexagons H and lines L1. With increasing a, the flat surface becomes unstable at one of the solid lines bounding region F. The resulting pattern can be H, Q or L1, depending on χ. Hysteresis is shown by the dashed line; in region H/F both H and F are stable, and similarly for Q/F. The solid line separating L1 and Q shows the transition L1 to Q, with hysteresis shown by the dashed line; in region Q/L1 both Q and L1 are stable. The grey band separating H and Q is a region of competition in which the two patterns coexist and/or oscillate slowly. Region D indicates a dynamic and/or disordered state; the transition from an ordered quasi-pattern to D (the grey band separating Q and D) involves slow, irregular dynamics in which the quasi-pattern spontaneously breaks up and reforms.

hexagons-to-lines transition takes place over a finite range of μ where the two patterns coexist, as in figure 15.

5.2. *Quasi-patterns and solitary waves*

For $\phi = 75°$, a twelvefold quasi-pattern is observed near the wavenumber bicriticality at $\chi \approx 65°$. Figure 16 shows the phase diagram. The intersection of the two solid lines is the bicritical point. The quasi-pattern Q can arise via a finite-amplitude transition
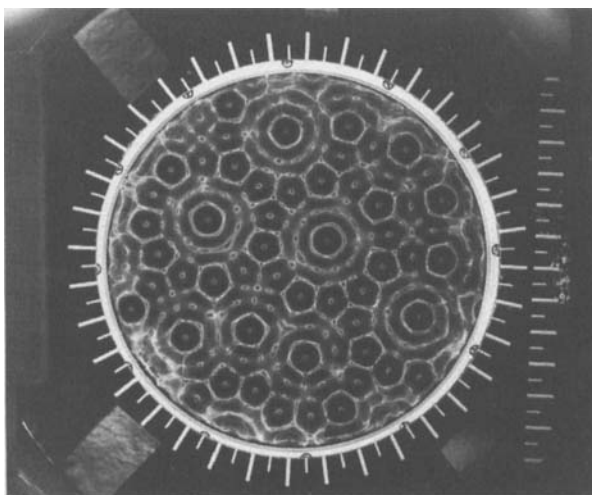
FIGURE 17. Quasi-pattern of twelvefold symmetry. Photograph of the pattern Q, which has long-range order but no spatial periodicity. The long-range order may be seen by viewing the photograph at a glancing angle; in certain directions there are parallel lines which traverse the container. The parameters are as in figures 12 and 16 with $\chi = 65°$.
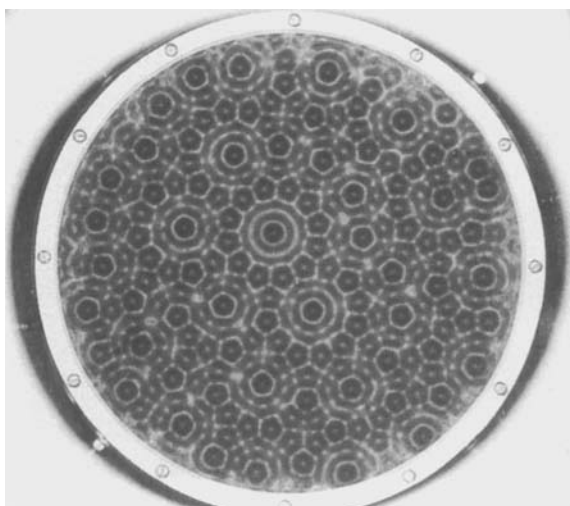

FIGURE 18. Higher-frequency quasi-pattern. The existence of Q does not depend strongly on frequency. Here $\omega/2\pi = 28$ Hz, $\phi = 68.4°$ and $\chi = 72°$.

directly from the flat surface F, or alternatively as a secondary transition from either hexagons H or lines L1. Figure 17 is a photograph of Q. It is stationary only for a small range of μ, above which it becomes dynamic and disordered.

The twelvefold quasi-pattern is observed over a range of frequencies. Figure 18 shows the result at higher frequency. The existing apparatus does not permit careful study at high frequency because the high critical forcing amplitude overheats the vibration exciter. The pattern in figure 18 was stationary for several seconds (after which the vibration exciter's protection system automatically disconnected it from the power amplifier).
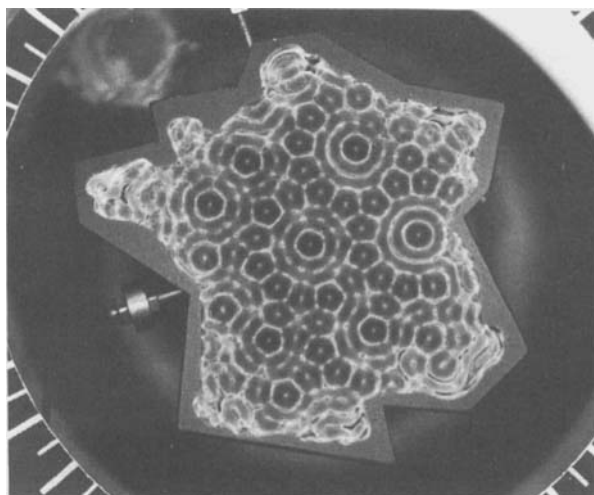
FIGURE 19. Quasi-pattern in irregular container. The sidewalls follow the outline of a map of France. The distance Bordeaux–Geneva is approximately 5 cm, and the depth is 3 mm. The irregular sidewall does not disrupt the quasi-crystalline order.
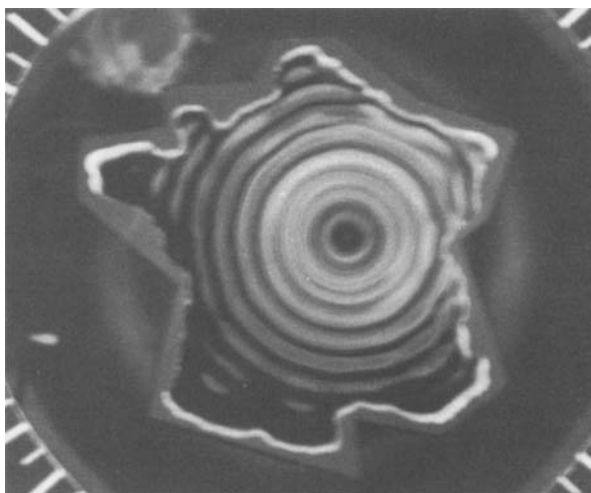

FIGURE 20. Solitary wave. These axisymmetric standing waves are observed near the lower hysteresis boundary when most of the quasi-pattern has collapsed to the flat surface. To stabilize these solitary waves it is necessary to slightly increase the forcing amplitude at the appropriate moment when one or several solitary waves remain. They remain stable with no horizontal velocity for up to five minutes.

To test the sidewall independence of the quasi-pattern, containers of several shapes were substituted, including square, hexagonal, octagonal shapes and a container whose sidewalls follow the irregular borders of a map of France (figure 19). The quasicrystalline order is not disrupted by the irregular shape outside of a small healing length near the sidewall.

Solitary waves as in figure 20 are sometimes observed near the lower boundary of the hysteresis loop (the dashed line in figure 16), especially when ϕ is a few degrees less than 75°.
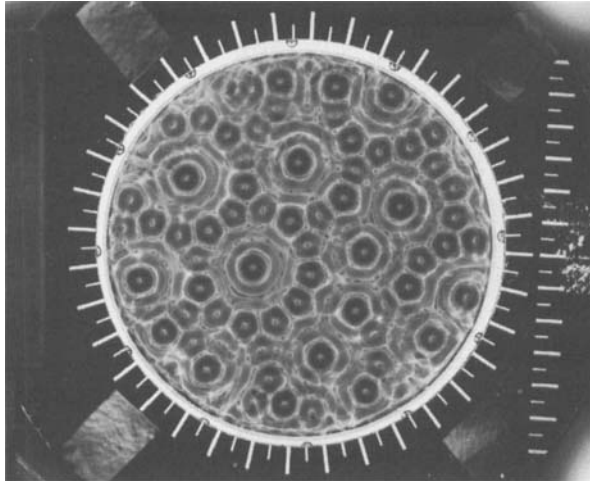
FIGURE 21. Quasi-pattern observed with frequency ratio 6/7. Similar twelvefold quasi-patterns are observed for frequency ratios 4/7 and 8/9. They are found by experimentally locating the bicritical mixing angle χ and then slowly varying the phase ϕ, with a fixed just above the stability threshold.
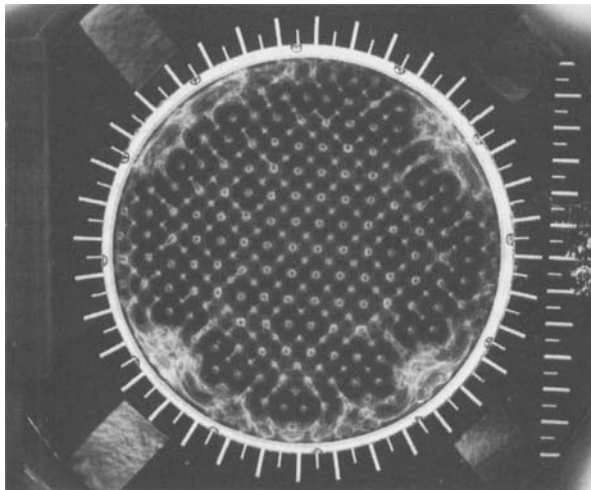

FIGURE 22. Squares observed with the frequency ratio 3/5. At this viscosity, the individual frequencies each produce lines; mixing the two frequencies results in squares for broad parameter ranges of χ and ϕ.

5.3. *Other frequency ratios*

Hexagons and twelvefold quasi-patterns are also observed for several even/odd frequency combinations, when the smaller frequency is even. Figure 21 exhibits a quasi-pattern observed with frequency ratio 6/7, and similar quasi-patterns are observed for 4/7 and 8/9.

With the odd/odd combination 3/5, squares can be observed even though the viscosity is high enough to favour lines for each frequency separately. Figure 22 is a photograph of such a square pattern.

5.4. *Discussion*

The existence of hexagons as the primary pattern over wide ranges of ϕ and χ, as shown in figure 11, is consistent with the presence of quadratic terms (triad interactions) in the amplitude equations (14) for even/odd forcing.
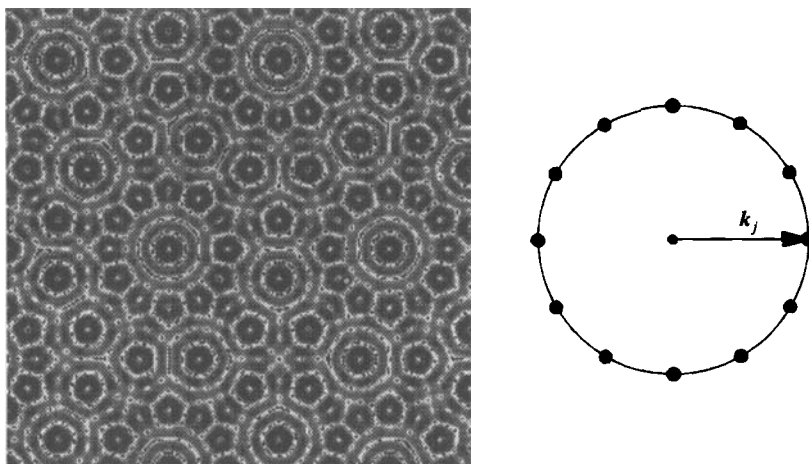
FIGURE 23. Computer-generated quasi-pattern is a linear superposition of twelve wavevectors k_j. The effect of the experimental visualization is approximated by time-averaging the reflected light that would reach the camera from each point on the surface. No fivefold or tenfold symmetry exists, despite the apparent pentagons.

The value $\phi = 15°$ in figure 11, at which hexagons are least easily produced, is interpreted as the value ϕ_0 for which $\alpha = 0$. In the case $m = 4$, $n = 5$ it can be shown that such a value must exist in the interval $0 \leqslant \phi \leqslant \pi/2$.

Since $\alpha \sim [a \sin \chi]^2$ and since the theory of hexagons and lines predicts that stable hexagons are found in a μ-interval of size $\sim \alpha^2$, the absence of hexagons for small χ is not surprising. If the triad interactions become very weak, they will not be able to compete with sidewall boundary effects and unavoidable inhomogeneities in the fluid and experimental apparatus, and the band of stable hexagons becomes smaller than the fluctuations of the stability threshold due to temperature. Where triad interactions are strong enough to result in clearly defined transitions, the size of the μ interval for which hexagons are stable appears to be proportional to $[a \sin \chi]^2$ as shown in figure 14. This contradicts the expected result for the case $m = 4$, $n = 5$, where α should be proportional to $[a \sin \chi]^2$ and thus the μ-intervals should have width $\sim \alpha^2 \sim [a \sin \chi]^4$.

The location of the wavenumber bicriticality, indicated by the solid line in figure 11, is not strongly sensitive to ϕ, varying only by $\pm 0.5°$. This result is in quantitative agreement with linear stability computations (Tuckerman *et al.* 1994).

Although the experimental quasi-pattern apparently exhibits small pentagons, there is no long-range fivefold or tenfold order. To see this, the expected appearance of the twelvefold standing-wave surface

$$\zeta(x, t) = A \sin(\omega t) \sum_{j=1}^{6} \exp(i k_j \cdot x) + \text{c.c.} \tag{23}$$

is computed, taking into account the experimental illumination. At each point where $\nabla \zeta$ is such that light would be reflected into the camera, the point is made white, otherwise it is black. The result is time-averaged over the assumed sinusoidal response, yielding grey levels, and A is adjusted to match the experimental photographs. The resulting figure 23 is to be compared with figures 17, 18 and 19. Even though by construction (23) has only twelvefold order, small pentagons are still apparent.

Observation of the twelvefold quasi-pattern in containers of different shapes indicates that it is not due to finite-size effects. This suggests that quasi-patterns of any

size could be produced experimentally if sufficiently powerful vibration exciters were used.

The relationship between the quasi-pattern and the solitary waves is not clear.

For the case of odd/odd forcing, Floquet multipliers other than -1 do not occur, and thus no triad interactions are available to favour hexagons or a twelvefold quasi-pattern. The observation of squares is not surprising under such circumstances, but the detailed mechanism has not been elucidated. It may be speculated that the wavenumbers associated with 5ω and with 3ω are approximately in the ratio $\sqrt{2}$ and thus an interaction like that of figure 4, but with $\theta_{ij} = \pi/2$, may be involved.

6. Conclusions

Many patterns are observed with two-frequency parametric forcing. The observation of parallel lines at high viscosity is as yet unexplained, but a similar observation in CO_2 near the liquid–vapour critical temperature suggests that high dissipation may be responsible. Hexagons are understood to be the result of weak triad interactions associated with the absence of the subharmonic symmetry in the case of even/odd forcing. The twelvefold quasi-pattern, while it occurs for parameter values near the wavenumber bicriticality, is found stroboscopically to be harmonic with respect to the total period of the forcing. Thus the role of the second wavenumber, which responds subharmonically, is not clear.

In all of these investigations study has been restricted to the primary instability of the flat surface. Some of the results are in agreement with the predictions of cubic-order amplitude equations for certain sets of critical wavevectors. The hope is raised that a reduction of the hydrodynamic problem can explain these patterns *ab initio*. This is especially interesting for the quasi-pattern since it appears that quasi-crystalline order can be completely and quantitatively characterized in this instance.

The present work motivates further studies with two or more frequencies. A very interesting example is the recent work of Müller (1993*b*) in which triangles have been observed with two- and three-frequency forcing, confirming for the first time the prediction of triangles by Golubitsky *et al.* (1984). More generally, it can be anticipated that competition among patterns will be easily arranged by deliberate mixing of waveforms. The multiple-frequency Faraday experiment is perhaps the most convenient and flexible system with which to study two-dimensional pattern formation and dynamics.

REFERENCES

BENJAMIN, T. B. & SCOTT, C. 1979 *J. Fluid Mech.* 2, 241.

BENJAMIN, T. B. & URSELL, F. 1954 *Proc. R. Soc. Lond.* A 255, 505.

BODENSCHATZ, E., BRUYN, J. R. DE, AHLERS, G. & CANNELL, D. S. 1991 *Phys. Rev. Lett.* 67, 3078.

CHRISTIANSEN, B., ALSTROM, P. & LEVINSEN, M. T. 1992 *Phys. Rev. Lett.* 68, 2157.

CILIBERTO, S., COULLET, P., LEGA, J., PAMPALONI, E. & PEREZ-GARCIA, C. 1990 *Phys. Rev. Lett.* 65, 2370.

CROQUETTE, V. 1989*a* *Contemp. Phys.* **30**, 113.

CROQUETTE, V. 1989*b* *Contemp. Phys.* **30**, 153.

CROSS, M. C. & HOHENBERG, P. C. 1993 *Rev. Modern Phys.* **65**, 851.

DOUADY, S. 1989 PhD thesis, Université de Paris VI.

DOUADY, S. 1990 *J. Fluid Mech.* **221**, 383.

DOUADY, S. & FAUVE, S. 1988 *Europhys. Lett.* **6**, 221.

EDWARDS, W. S. & FAUVE, S. 1992 *C. R. Acad. Sci. Paris* **315**(II), 417.

EDWARDS, W. S. & FAUVE, S. 1993 *Phys. Rev.* E **47**, R788.

EZERSKII, A. B., RABINOVICH, M. I., REUTOV, V. P. & STAROBINETS, I. M. 1986 *Zh. Eksp. Teor. Fiz.* **91**, 2070 (*Sov. Phys. JETP* **64**, 1228).

FARADAY, M. 1831 *Phil. Trans. R. Soc. Lond.* **52**, 319.

FAUVE, S., KUMAR, K., LAROCHE, C., BEYSENS, D. & GARRABOS, Y. 1992 *Phys. Rev. Lett.* **68**, 3160.

GLUCKMAN, B. J., MARCQ, P., BRIDGER, J. & GOLLUB, J. P. 1993 *Phys. Rev. Lett.* **71**, 2034.

GOLUBITSKY, M., SWIFT, J. W. & KNOBLOCH, E. 1984 *Physica* **10D**, 249.

KUMAR, K. & TUCKERMAN, L. S. 1994 Parametric instability at the interface of two fluids. *J. Fluid Mech.* **279**, 49–68.

LANDAU, L. D. & LIFSHITZ, E. M. 1976 *Course of Theoretical Physics*; *Vol. 1, Mechanics*, 3rd edn. Pergammon.

LANDAU, L. D. & LIFSHITZ, E. M. 1987 *Course of Theoretical Physics*; *Vol. 2, Fluid Mechanics*, 2nd edn. Pergammon.

MALOMED, B. A., NEPOMNYASHCHIĬ, A. A. & TRIBELSKIĬ, M. I. 1989 *Sov. Phys. JETP* **69**, 388.

MERMIN, N. D. & TROIAN, S. M. 1985 *Phys. Rev. Lett.* **54**, 1524.

MILES, J. 1993 *J. Fluid Mech.* **248**, 671.

MILNER, J. 1991 *J. Fluid Mech.* **225**, 81.

MÜLLER, H. W. 1993*a* *Phys. Rev.* E **49**, 1273.

MÜLLER, H. W. 1993*b* *Phys. Rev. Lett.* **71**, 3287.

NEWELL, A. C., PASSOT, T. & LEGA, J. 1993 *Ann. Rev. Fluid Mech.* **25**, 399.

NEWELL, A. C. & POMEAU, Y. 1993 *J. Phys.* A **26**, L429.

PALM, E. 1960 *J. Fluid Mech.* **8**, 183.

PAMPALONI, E., PEREZ-GARCIA, C., ALBAVETTI, L. & CILIBERTO, S. 1992 *J. Fluid Mech.* **234**, 393.

TUCKERMAN, L. S., KUMAR, K. & EDWARDS, W. S. 1994 in preparation.

TUFILLARO, N. B., RAMSHANKAR, R. & GOLLUB, J. P. 1989 *Phys. Rev. Lett.* **62**, 422.

ZIPPELIUS, A. & SIGGIA, E. D. 1983 *Phys. Fluids* **26**, 2905.